ACS OMEGA

Open Access

http://pubs.acs.org/journal/acsodf

Article

Fluorescence Modulation in UiO-66-NH_2 via Photooxidation and Selective Reduction

Yongdeok Ahn,* Minsoo Park, Younghu Son, Juhyeong Cho, Min Jeong Park, Daeha Seo,* and Minyoung Yoon*

Cite This: *ACS Omega* 2025, 10, 42882−42891

Read Online

ACCESS | Metrics & More | Article Recommendations | Supporting Information

ABSTRACT: Metal−organic frameworks with emissive ligands offer tunable photophysical properties that are sensitive to their coordination environment and structural configuration. In this study, we demonstrate that the fluorescence of UiO-66-NH_2 can be modulated through photo-oxidation-induced quenching and subsequent solvent-mediated recovery. Upon visible-light irradiation, reactive oxygen species induce two distinct oxidation pathways: irreversible oxidation of the ligand and reversible oxidation of the metal-oxo cluster. These redox events lead to partial disruption of the coordination environment and result in fluorescence loss. Reduction using mild alcohols selectively removes adsorbed oxidative species from $Zr_6O_4(OH)_4$, leading to partial recovery of fluorescence and porosity. The extent of fluorescence restoration correlates with both the reducing strength and molecular size of the alcohol, reflecting its ability to penetrate internal pores and access to redox-active sites. Notably, some alcohol-treated samples exhibited nitrogen uptake beyond that of pristine UiO-66-NH_2, suggesting redux-induced structural reorganization and defect-assisted pore expansion. These results establish a structure−function relationship in MOFs governed by localized redox chemistry, providing a platform for designing reconfigurable optical materials with switchable photophysical and porous characteristics.

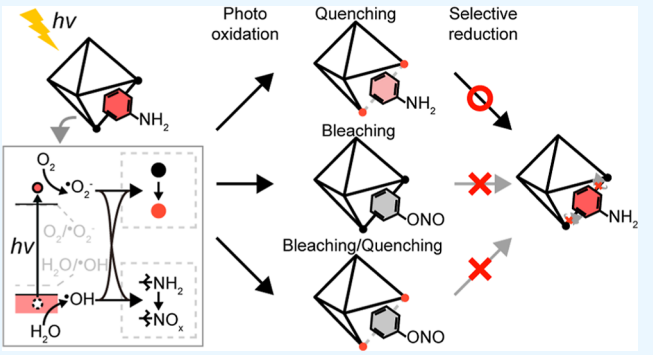

INTRODUCTION

Metal−organic frameworks (MOFs), a subclass of porous crystalline materials, offer exceptional chemical tunability and structural diversity, making them highly attractive for applications in sensing, catalysis, gas storage, and drug delivery.[1−4] Beyond their high porosity and modular construction, MOFs have recently garnered attention for their potential in photonic and optoelectronic applications, particularly when functionalized with emissive ligands (L_{em}).[5−9] In such systems, the fluorescence properties are closely tied to the structural coordination change of the framework, which governs nonradiative decay pathways such as intramolecular motions and $\pi-\pi$ stacking.[10−13]

A key mechanism underlying fluorescence modulation in MOFs is restricted intramolecular motion (RIM), wherein the rigid coordination between metal clusters and organic ligands suppresses dynamic molecular motions and enhances radiative recombination.[14−16] However, this coordination change is not static. Localized environmental stimuli, such as photoexcitation or exposure to reactive oxygen species (ROS), can induce oxidation at specific framework sites, dynamically altering coordination interactions and reducing structural coordination.[17] These redox-induced changes can trigger fluorescence quenching and framework deformation, yet their reversibility and structural implications remain insufficiently understood.

Herein, we present a system in which dual oxidation pathways—irreversible oxidation of L_{em} and reversible oxidation of metal-oxo clusters (M_{oxo})—can be selectively controlled to modulate both the coordination and the photoluminescence (PL) of the emissive MOF (MOF_{em}). Using real-time fluorescence microscopy combined with bulk spectroscopic and structural analysis, we demonstrate that light-induced ROS generation leads to fluorescence loss via local oxidation.[18] Subsequent treatment with alcohol-based reductants enables partial recovery of the fluorescence and structure by selectively reversing the oxidation of M_{oxo}, while the oxidized L_{em} remains unaltered.

This redox-mediated tuning of coordination provides a new strategy for dynamic modulation of the MOF photophysical behavior. Moreover, we show that the extent of fluorescence

Received: June 11, 2025
Revised: August 23, 2025
Accepted: September 10, 2025
Published: September 15, 2025

recovery correlates with the strength of the reductant. These findings establish a structure−property relationship in which local oxidation−reduction events directly influence optical output and physical coordination change, offering a versatile platform for designing responsive and reconfigurable MOF-based systems.

EXPERIMENTAL SECTIONS

Materials. Zirconium(IV) tetrachloride (99.5%, Sigma-Aldrich), 2-nitroterephthalic acid (BDC-NO2, 98%, Tocho Chemical Industry), 2-aminoterephthalic acid (BDC-NH2, 98%, Tocho Chemical Industry), dimethylformamide (DMF, 99%, Sigma-Aldrich), methanol (99.8%, Sigma-Aldrich), ethanol (99.8%, Sigma-Aldrich), propanol (99.8%, Sigma-Aldrich), *N*,*N*-dimethylformamide (99.5%, Samchun Chemicals), and hydrochloric acid (Samchun Chemicals) were obtained. All chemicals and solvents were used without further purification.

Characterization. UV−vis spectra were recorded on a diode array spectrophotometer (Agilent, Cary 8454). Emission spectra were collected through photoluminescence spectroscopy (BioTek, Synergy H1). 1H spectra were measured with Fourier-transform nuclear magnetic resonance spectrometry (FT-NMR, Bruker, AVANCE III 400). ^{1}H NMR chemical shifts are reported in ppm (δ) relative to the residual solvent with the solvent resonance employed as an internal standard (CD3)2SO, δ 2.50 ppm. Data are presented as follows: chemical shift, multiplicity (s = singlet, d = doublet, t = triplet, q = quartet, m = multiplet), coupling constants (Hz), and integration.

X-ray diffraction (XRD) data were collected by using the Empyrean X-ray diffractometer (Panalytical) with Cu Kα1 radiation (λ = 1.541 Å, 40 kV, and 30 mA). X-ray photoelectron spectroscopy (XPS) analyses were conducted using a Thermo Scientific ESCALAB 250Xi instrument with a monochromatized Al Kα line source. Fourier-transform infrared (FTIR) analyses were conducted by FTIR spectroscopy (Thermo Scientific, Nicolet Continuum).

Nitrogen adsorption isotherms were measured at 77 K by using a Micromeritics ASAP 2020 analyzer with high-purity nitrogen gas (99.999%). The fluorescence microscope was equipped with a laser (Nikon, LU-N4 Laser Unit, 405 nm) to UiO-66-NH_2 at its respective excitation wavelength, a perfect focus system (PFS, TI2-N-ND-P), a motorized stage, and an electron multiplying charge-coupled device (EMCCD, Andor, iXorn Ultra 897) at its respective excitation wavelength. All microscopic images were observed under a 10× objective lens.

Synthesis of UiO-66-NH_2. The amino-functionalized Zr-based MOF, UiO-66-NH_2, was synthesized via a solvothermal method.[19−21] 2-Aminoterephthalic acid (0.27 g, 1.50 mmol) was dissolved in 15 mL of DMF and stirred in a glass bottle. Separately, $ZrCl_4$ (0.25 g, 1.08 mmol) was dissolved in 15 mL of DMF and added to the ligand solution. Then, 2.5 mL of concentrated HCl was introduced into the mixture. The resulting solution was transferred to a Teflon-lined stainless-steel autoclave and heated at 120 °C for 24 h in a convection oven. After cooling to room temperature, the precipitate was collected by centrifugation at 6500 rpm for 10 min and washed three times with fresh DMF. To remove DMF from the MOF pores, the solid was soaked in methanol, with solvent exchanged three times over 3 days. The final product was dried at 120 °C under dynamic vacuum by using a Schlenk line and stored in a glass vial.

Synthesis of UiO-66-NO_2. The nitro-functionalized Zr-based MOF, UiO-66-NO_2, was synthesized via a solvothermal method.[22] $ZrCl_4$ (0.125 g, 0.54 mmol) and NO_2−H_2BDC (0.158 g, 0.75 mmol) were dissolved in 20 mL of DMF and 2.5 mL of concentrated HCl in a 30 mL glass bottle. The mixture was sonicated at room temperature for 15 min to ensure complete dissolution. The resulting clear solution was transferred to a Teflon-lined stainless-steel autoclave and heated at 100 °C for 24 h in a convection oven. After it was cooled to room temperature, the suspension was centrifuged at 6500 rpm for 15 min to collect the precipitate. The solid was washed three to four times with ethanol to remove unreacted precursors. A further activation step was performed by soaking the product in ethanol for 1 week, replacing the solvent daily. Finally, the MOF was dried at 120 °C under dynamic vacuum using a Schlenk line and stored in a glass vial.

Oxidation of UiO-66-NH_2 and Reduction of ox-UiO-66-NH_2. For inducing oxidation of UiO-66-NH_2, 100 mg of UiO-66-NH_2 was plated on 35 mm glass-bottom dishes (P35G-0−10-C, MatTek, Ashland, MA, USA). The plated UiO-66-NH_2 was exposed to white light emitted from a mercury lamp (Nikon, C-HGFIE Intensilight) for 1 h, resulting in a visibly darker color due to photooxidation. The samples were allowed to equilibrate to room temperature to eliminate thermal effects resulting from light irradiation. This process was repeated three times.

For reduction of ox-UiO66-NH_2, alcohols (methanol, ethanol, and propanol) were used as a mild reductant. ox-UiO-66-NH_2 was aged with 2 mL of alcohol for 12 h at room temperature. After aging, red-UiO-66-NH_2 was fully dried over 48 h under vacuum and stored in the dark condition.

Observation of Fluorescence Intensity Using Fluorescence Microscopy. The oxidation and reduction of UiO-66-NH_2 were observed by changes in the fluorescence intensity. 0.1 mg of UiO-66-NH_2 was plated onto washed 35 mm glass-bottom dishes after the sample was washed three times with ethanol and dried under vacuum for 48 h. The oxidation of UiO-66-NH_2 and reduction of ox-UiO-66-NH_2 were monitored and imaged using fluorescence microscopy with a 405 nm laser. Snapshots were captured with 1 and 2 min intervals for oxidation and reduction, respectively. All imaging data from fluorescence microscopy were processed and analyzed by using ImageJ software.

Measurement of Fluorescence Intensity at the Bulk Level. Bulk level fluorescence intensities were evaluated by PL spectroscopy under excitation at λ_{max} = 405 nm for MOFs and λ_{max} = 350 nm for BDC−NH_2. The idealized chemical formula of UiO-66-NH_2 is $Zr_6O_4(OH)_4(BDC{-}NH_2)_6$, comprising one Zr-based secondary building unit (SBU) and six BDC−NH_2 linkers. Based on the atomic weights of Zr (91.22 g/mol), O (16.00 g/mol), H (1.008 g/mol), C (12.01 g/mol), and N (14.01 g/mol), the molecular weight of the inorganic $Zr_6O_4(OH)_4$ cluster is 679.36 g/mol. Each BDC−NH_2 ligand has a molecular weight of 181.15 g/mol, leading to a combined mass of 1086.90 g/mol for the six ligands. Therefore, the total molecular weight of the defect-free UiO-66-NH_2 unit is 1766.12 g/mol. On a mass basis, the theoretical BDC−NH_2 content is calculated as

$$\frac{1086.90}{1766.26} \times 100 \approx 61.5\%$$

while the $Zr_6O_4(OH)_4$ accounts for the remaining 28.5%. Accordingly, we compared the fluorescence intensity of 0.1 g of

https://doi.org/10.1021/acsomega.5c05521
ACS Omega 2025, 10, 42882−42891

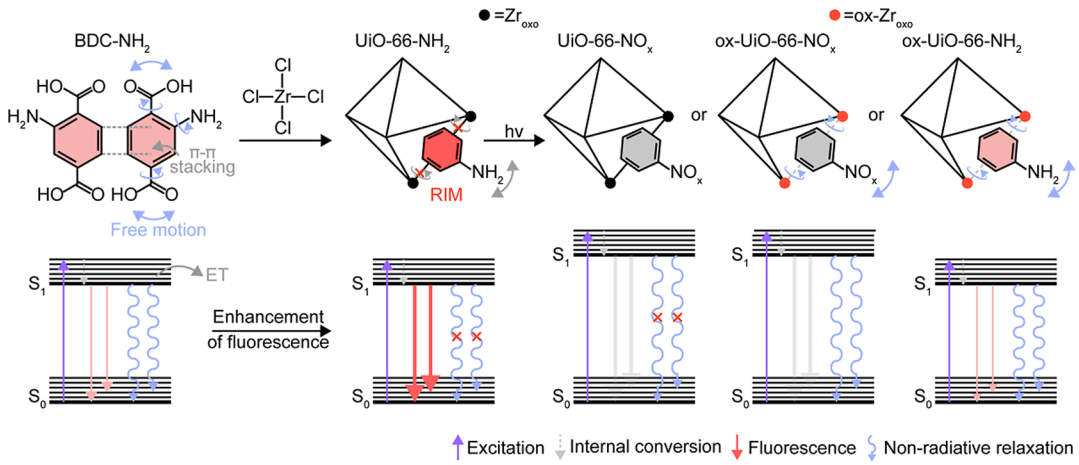

Figure 1. Schematic illustration of photooxidation-induced fluorescence quenching and selective reductive recovery in UiO-66-NH_2. Visible-light irradiation generates ROS, which initiate dual-site oxidation within the MOF framework. BDC−NH_2 undergoes irreversible oxidation to BDC−NO_x (NO_x = −ONO or $-NO_2$), disrupting π-conjugation and eliminating fluorescence emission. Concurrently, ROS transiently adsorb onto Zr_{oxo}, inducing changes in metal−ligand coordination that lead to structural rearrangement and fluorescence quenching. Subsequent treatment with mild alcohols selectively removes the adsorbed ROS from Zr_{oxo}, partially restoring coordination, structural order, and fluorescence. The ligand oxidation remains irreversible, while cluster oxidation is reversible, enabling redox-mediated modulation of MOF fluorescence and porosity.

UiO-66-NH_2 with that of 0.0615 g of BDC−NH_2, which corresponds to the theoretical mass of the ligand present in the MOF. Furthermore, to minimize $\pi-\pi$ stacking of BDC−NH_2, we performed sonication in ethanol for 20 min prior to PL measurement.

The red-shifted emission observed for the molecular (noncoordinated) BDC−NH_2 is likely attributed to $\pi-\pi$ stacking interactions in the aggregated state, which can induce exciton delocalization and lower the energy of the emissive state.

BET Measurements. Gas adsorption isotherms at 77 K were recorded with a high-purity nitrogen gas (99.999%). Prior to analysis, the samples were degassed at 130 °C under a vacuum for 24 h. The specific surface areas were calculated by using the Brunauer−Emmett−Teller (BET) method, implemented through the Micromeritics analysis software.

Statistical Analysis. All data are represented as the mean ± s.d. of indicated replicates. Statistical analysis was performed using GraphPad Prism 8.0 software with a two-side paired *t*-test.

RESULTS AND DISCUSSION

Fluorescence properties of MOFs are highly sensitive to the local coordination environment and structural coordination changes surrounding the L_{em}. We employed UiO-66-NH_2 as a model system containing two different oxidizable moieties: 2-aminoterephthalic acid (BDC−NH_2) and $Zr_6O_4(OH)_4$ (Zr_{oxo}), referred to as Lem and M_{oxo}, respectively (Figure S1).[23−25] For instance, when free ligand BDC−NH_2 is incorporated into the rigid UiO-66-NH_2 framework, both intramolecular motions and $\pi-\pi$ stacking are significantly restricted. This confinement suppresses nonradiative decay pathways and enhances radiative recombination, as described by the RIM mechanism. The PL spectrum of UiO-66-NH_2 displays an ∼1.5-fold increase in intensity and a notable blue shift compared to free BDC−NH_2, confirming the coordination change-induced enhancement of fluorescence (Figure S2). These results underscore the importance of metal−ligand coordination in stabilizing the emissive state by enforcing structural coordination change.[26,27] Conversely, disruption of coordination between BDC−NH_2 and Zr_{oxo} can restore molecular freedom, reopen nonradiative channels, and reduce fluorescence.[28]

Figure 1 conceptually illustrates how redox-induced structural changes modulate the MOF fluorescence. Upon visible-light irradiation, ROS can selectively oxidize either BDC−NH_2 or Zr_{oxo}. In the case of ligand oxidation, amine groups are irreversibly converted to the nitro ($-NO_2$) or nitrito group (−ONO), which changes the coordination and alters the electronic structure, effectively modifying the bandgap.[29] This chemical transformation leads to the loss of radiative transitions and often results in complete fluorescence quenching due to the dominance of nonradiative decay or lack of emissive states. In contrast, oxidation of Zr_{oxo} involves transient adsorption of ROS, which weakens metal−ligand coordination and relaxes the rigid scaffold.[30,31] This structural softening increases vibrational degrees of freedom and reactivates nonradiative decay pathways without fundamentally disrupting the electronic structure of L_{em}. As a result, the fluorescence intensity decreases, but residual emission may persist.

Thus, ligand oxidation results in permanent photophysical degradation, whereas cluster oxidation leads to a partial fluorescence loss driven by structural change. These distinct outcomes form the basis of our hypothesis: selective reduction of oxidized M_{oxo} should partially restore the original coordination and, consequently, the fluorescence.

UiO-66-NH_2 demonstrates a bandgap of approximately 2.9 eV, facilitating photoactivation under visible light (Figure 2a). Upon irradiation, the excited electron−hole pairs recombine, resulting in fluorescence emission. The valence band (VB) and conduction band (CB) of UiO-66-NH2 are known to be positioned at approximately +2.5 V and −0.3 V versus the normal hydrogen electrode (NHE), respectively.[29,32] These band-edge potentials are adequate to reduce dissolved O_2 to superoxide radicals ($O_2^{\bullet-}$, −0.33 V vs NHE) and oxidize H_2O to hydroxyl radicals ($^{\bullet}OH$, +2.4 V vs NHE), thereby generating ROS within UiO-66-NH_2.[33]

We hypothesize that these ROS species facilitate two distinct oxidation pathways in UiO-66-NH_2 to generate oxidized UiO-

https://doi.org/10.1021/acsomega.5c05521
ACS Omega 2025, 10, 42882−42891

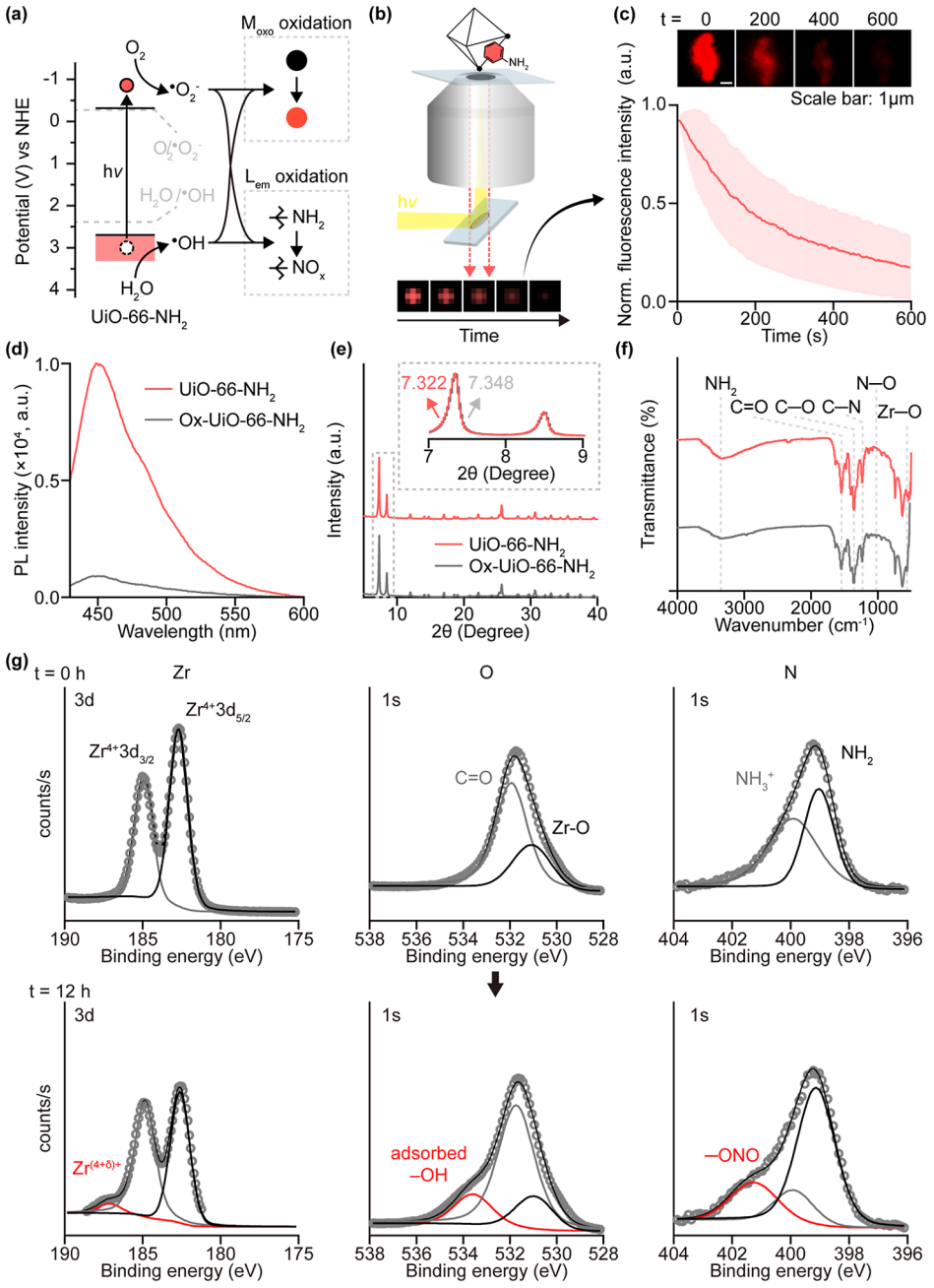

Figure 2. Experimental verification of photooxidation-induced structural and photophysical changes in UiO-66-NH_2. (a) Band energy diagram of UiO-66-NH_2, indicating that the CB and VB are sufficient to generate ROS under visible-light irradiation. (b) Schematic illustration of the experimental setting for single-level observation. (c) Time-lapse fluorescence microscopy images (top) and fluorescence intensity (bottom) showing photobleaching of UiO-66-NH_2 particles under light exposure. Pink indicates standard deviation. While the fluorescence emission peak is observed at ∼450 nm, corresponding to the blue region of the visible spectrum, red pseudocolor was applied in the image to enhance visual clarity and contrast. (d) Bulk PL spectra showing significant fluorescence quenching after irradiation. (e) XRD pattern showing a slight peak shift toward higher 2θ after photooxidation, indicating minor lattice contraction. (f) FTIR spectra revealing the disappearance of NH_2 stretching peaks and the appearance of new Zr−O and C−H related bands, consistent with oxidation of both BDC−NH_2 and Zr_{oxo}. (g) XPS spectra confirming the formation of Zr_{oxo}, adsorbed ROS, and −ONO, indicating oxidation of both structural domains.

66-NH_2 (ox-UiO-66-NH_2). $^{\bullet}OH$ and $O_2^{\bullet-}$ irreversibly oxidize BDC−NH_2 into BDC−ONO, while being reversibly adsorbed onto Zr_{oxo}, thereby promoting further oxidation of Zr_{oxo} (ox-Zr_{oxo}).[34−36] Free BDC−NH_2 molecules that were not incorporated into the MOF crystalline framework did not undergo photoinduced oxidation, indicating that the observed oxidative reactivity is an intrinsic property of the MOF architecture (Figure S3). Notably, these events manifest as photobleaching (irreversible oxidation of BDC−NH_2) and fluorescence quenching (reversible oxidation at Zr_{oxo}), both contributing to the overall decrease in fluorescence. Real-time fluorescence microscopy revealed significant quenching under visible light under air conditions, consistent with ongoing photo-oxidation processes (Figure 2b,c). This photobleaching was observed by PL spectroscopy at the bulk level (Figure 2d). Additionally, a discernible color change in the crystals further underscored the chemical transformations taking place (Figure S4).

https://doi.org/10.1021/acsomega.5c05521
ACS Omega 2025, 10, 42882−42891

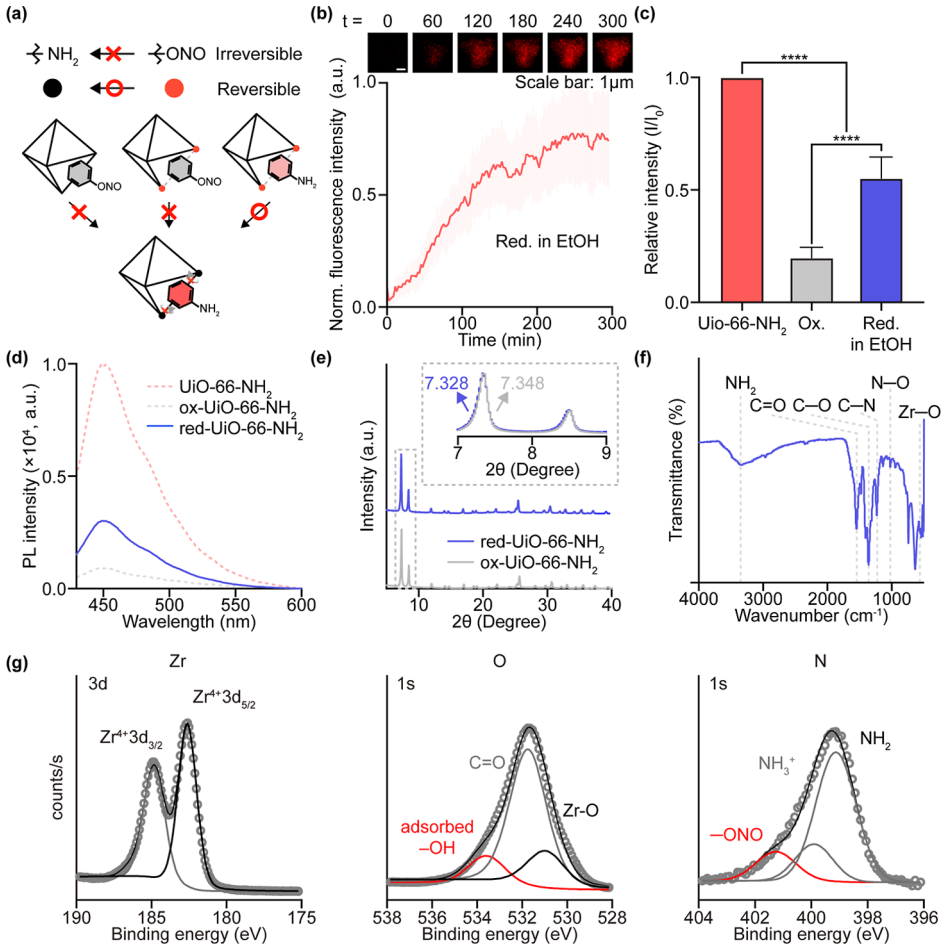

Figure 3. Selective recovery of the fluorescence and partial structure in ox-UiO-66-NH_2 via EtOH aging. (a) Schematic illustration of reduction pathways in ox-UiO-66-NH_2, showing irreversible reduction of $-NO_x$ and reversible ox-Zr_{oxo}. (b) Time-lapse fluorescence microscopy images (top) and fluorescence intensity (bottom) showing partial fluorescence recovery of single ox-UiO-66-NH_2 in EtOH. Pink indicates standard deviation. To facilitate visual interpretation, the fluorescence originating at ∼450 nm (blue emission) was displayed in red in the imaging data. (c) Statistical analysis of fluorescence intensity obtained from fluorescence microscopy observation. (d) Bulk PL spectra showing significant fluorescence recovery after reduction in EtOH. (e) XRD patterns showing partial reversal of the photooxidation-induced peak shift, indicating lattice reconstruction after EtOH treatment. (f) FTIR spectra of red-UiO-66-NH_2. (g) XPS spectra of red-UiO-66-NH_2 supporting the selective reduction of ox-Zr_{oxo}. ****$p < 0.0001$.

To confirm these oxidative modifications, we conducted X-ray diffraction (XRD) and Fourier-transform infrared (FTIR) spectroscopy measurements. XRD analysis revealed a shift in the main reflection corresponding to the (1 1 1) plane between 5° and 10° in 2θ, moving toward ∼7.348°, which corresponds to a slight contraction of the lattice constant by approximately 0.0738 Å (Figure 2e). This structural change underscores how chemical oxidation of both domains (ligand and cluster) can influence the overall crystalline framework.

Postirradiation FTIR spectra revealed four major changes (Figure 2f): (1) the disappearance of a prominent band in the 500−700 cm^{-1} range,[37,38] which may be attributed to local metal−ligand vibrational modes, (2 and 3) the emergence of new bands at ∼1020 and ∼2950 cm^{-1}, possibly indicating newly formed N−O and C−H or adsorbed oxidative species, respectively,[39] and (4) a marked decrease in the intensity of the N−H stretching region near 3200 cm^{-1}. These findings strongly suggest oxidation of both BDC−NH_2 and Zr_{oxo}, consistent with dual oxidation pathways. XPS provided further insight into changes in the oxidation states of N, O, and Zr (Figure 2g). After photobleaching, a new peak at ∼187 eV in the Zr 3d region suggests the presence of $Zr^{(4+\delta)+}$, indicative of partial oxidation beyond the conventional Zr^{4+} state.[36] The O 1s spectrum showed a new peak at ∼533.8 eV, corresponding to adsorbed ROS on Zr_{oxo}.[40−42] In the N 1s spectrum, the appearance of a peak at ∼401.8 eV is consistent with the formation of $-NO_2$ or −ONO from $-NH_2$.[39,43]

Together, these XPS data corroborate the FTIR observations, confirming that both L_{em} and M_{oxo} are oxidized under photoirradiation. Alternatively, as recently proposed by studies on Zr-based MOFs, such spectral shifts may also arise from photoexcited hole transfer from the ligand to the Zr_6 node without the formal reduction of Zr^{4+}. These results underscore the need for further investigation into multiple possible mechanistic pathways in MOF redox chemistry.[44] We monitored the temperature of the sample during light irradiation and confirmed that no significant thermal increase occurred during the exposure period. This result indicates that the photooxidation of UiO-66-NH_2 is not thermally driven but rather proceeds primarily through photoinduced generation of ROS. Hence, thermal effects can be considered negligible in the reaction mechanism (Figure S5).

To selectively reverse the two distinct oxidation pathways, irreversible ligand oxidation and reversible cluster oxidation, a

https://doi.org/10.1021/acsomega.5c05521
ACS Omega 2025, 10, 42882−42891

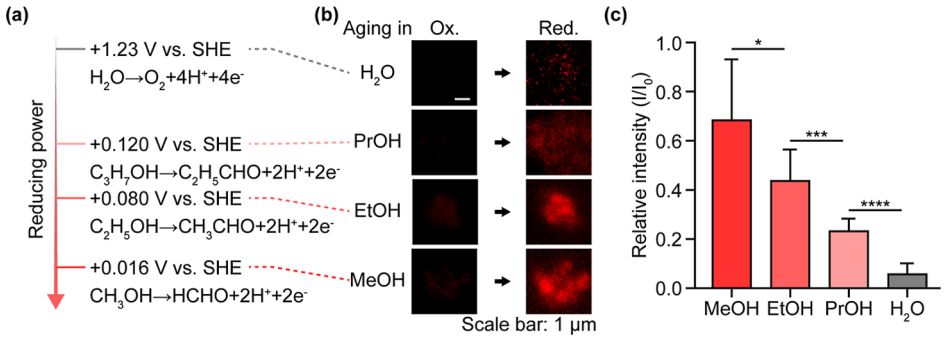

Figure 4. Dependence of fluorescence recovery on the reducing power of alcohols. (a) Schematic illustration of the reducing power of solvent. (b) Fluorescence microscopy images of ox-UiO-66-NH_2 treated with H_2O, PrOH, EtOH, and MeOH. Although the intrinsic emission occurs at ~450 nm (blue region), the fluorescence signal was visualized using red pseudocolor to ensure better visibility and distinguishability in the image. (c) Quantitative analysis of fluorescence recovery at the single-particle level. MeOH achieves the highest recovery (~70%), followed by EtOH (~50%), PrOH (~20%), and negligible recovery with H_2O. The trend is attributed to both the reducing power and molecular size of each alcohol, affecting their accessibility to internal redox-active sites. ****$p < 0.0001$, ***$p < 0.001$, *$p < 0.05$.

solvent-induced reduction strategy was employed, utilizing alcohols as mild reducing agents.[45] Although alcohols are not effective in reducing $-NO_2$ or $-ONO$ groups back to $-NH_2$ under mild conditions, they can facilitate the removal of adsorbed ROS on Zr_{oxo}, thereby restoring the partially oxidized metal domain (Figure 3a). Ethanol (EtOH) was specifically chosen due to its relatively small molecular size (~4.1 Å) and mild reductive ability,[46] which allows it to penetrate the 8−11 Å pores of UiO-66-NH_2 and interact with internal sites.[47,48]

Following the aging of the ox-UiO-66-NH_2 samples in EtOH, the MOF was reexamined using fluorescence microscopy, FTIR, XPS, and XRD analyses. We monitored the fluorescence recovery of ox-UiO-66-NH_2 during EtOH aging at the single-particle level (Figure 3b). Statistically, approximately 50% of the fluorescence intensity was restored, indicating partial structural recovery following the reduction of the oxidized domains (Figure 3c). Notably, the PL peak position of the recovered fluorescence remained unchanged compared to the pristine state, suggesting that the electronic structure of the ligands was preserved and that the fluorescence restoration primarily arose from the re-establishment of structural coordination (Figures 3d and S6).

To investigate the role of EtOH in the fluorescence recovery, we incubated ox-UiO-66-NH_2 in mixed solvents with varying water-to-EtOH volume ratios (Figure S7). As the EtOH content increased, an enhancement in fluorescence intensity was observed, reaching a maximum at 100% EtOH. This trend suggests that EtOH functions as a chemical reductant, facilitating the restoration of Zr_{oxo} environments required for fluorescence emissions.

The observed dependence is consistent with a redox mechanism in which EtOH donates electrons and protons to ox-Zr_{oxo} species, as illustrated in the following reactions

$$\text{ox} - Zr_{oxo} + CH_3CH_2OH \rightarrow Zr_{oxo} + CH_3CHO$$

These reactions restore the electron density and coordination state of Zr_{oxo}, thereby reactivating L_{em}-to-M_{oxo} charge transfer pathways and enabling fluorescence recovery. To evaluate the possibility of further oxidation to carboxylic acid beyond the alcohol-to-aldehyde transformation, we treated ox-UiO-66-NH_2 with formaldehyde (HCHO) (Figure S8).[49] No fluorescence recovery was observed, implying that the redox activity is confined to the $2H^+/2e^-$ step under our experimental conditions.[50]

These observations support the conclusion that the selective reduction of M_{oxo} reinstates the original coordination environment, reaffirming the tight correlation between the MOF coordination change and photophysical performance. This partial chemical restoration translated into a partial structural recovery, as evidenced by the XRD patterns (Figure 3e).

After EtOH aging, the main diffraction peaks of the reduced UiO-66-NH_2 (red-UiO-66-NH_2) were found to shift back toward UiO-66-NH_2 positions, although not fully coinciding with the ox-UiO-66-NH_2 positions. These data imply that while the metal cluster domain can be selectively reduced to some extent, the ligand domain undergoes permanent oxidation that contributes to a locally modified crystal lattice.

The FTIR results confirmed the initial hypothesis of selective reduction (Figure 3f). Although the previously diminished Zr−O peak (500−700 cm^{-1}) was recovered, the ~3200 cm^{-1} peak attributed to NH_2 stretching did not reappear, indicating that the $-NH_2$ to $-NO_2$ or $-NH_2$ to $-ONO$ transition in the organic linker could not be reversed under these conditions. Moreover, the newly generated N−O (~1020 cm^{-1}) and C−H bands (~2900 cm^{-1}) remained unchanged, suggesting that any oxidative byproducts or intermediate species in the L_{em} domain were not fully eliminated by EtOH treatment.

XPS analysis corroborated the FTIR findings (Figure 3g). The $Zr^{(4+\delta)+}$ peak at ~187 eV, associated with higher oxidation states, disappeared or was substantially reduced after EtOH aging, while the intensity of the adsorbed O_2 peak near ~533.8 eV also decreased significantly, reflecting the removal of surface-bound ROS on Zr_{oxo}. However, the newly formed $-NO_2$ peak near ~401.8 eV (indicative of the $-ONO$ or $-NO_2$ moiety) remained, confirming that L_{em} oxidation was indeed irreversible under these reaction conditions. Alternatively, considering the proton-rich reaction environment and the presence of redox-active linkers, the possibility of proton-coupled electron transfer (PCET) pathways at the MOF interface should also be considered, as discussed in recent reports.[51]

Overall, these results validate the initial hypothesis that two photooxidation pathways coexist, an irreversible one affecting the linker and a reversible one at Zr_{oxo}, and further demonstrate that such oxidative changes can promote structural transformations in MOFs.

https://doi.org/10.1021/acsomega.5c05521
ACS Omega 2025, 10, 42882−42891

The extent of fluorescence restoration in ox-UiO-66-NH_2 upon exposure to different alcohols was significantly influenced by both the physicochemical properties and molecular size of the alcohols (Figure 4a).[52] Fluorescence microscopy results demonstrated that alcohols with different reducing powers showed different fluorescence restorations of a single MOF (Figure 4b). Methanol (MeOH) restored approximately 70% of the fluorescence postquenching, while EtOH achieved about 50% and propanol (PrOH) only around 20%. H_2O and air show negligible restoration of the fluorescence (Figures 4c and S9). We attribute these variations to two primary factors: (i) molecular size, with MeOH (~3.4 Å) penetrating more rapidly and deeply into the 8−11 Å pores of UiO-66-NH_2, and (ii) reducing power as MeOH is generally regarded as a stronger mild reducing agent than EtOH or PrOH.

To assess the reducibility of the ligand component, we subjected UiO-66-NO_2 to alcohol aging and analyzed the resulting product using FTIR spectroscopy (Figure S10). No reduction of $-NO_2$ was detected under these conditions, indicating that the $-NO_x$ functionality in ox-UiO-66-NH_2 remains chemically intact in alcohol media. These findings further support the conclusion that fluorescence recovery in the ox-UiO-66-NH_2 system originates primarily from the selective reduction of oxidized metal clusters rather than ligand-based redox processes. These results strongly support our model, in which reduction of ox-Zr_{oxo} governs fluorescence restoration. Since $-NO_2$ and −ONO on L_{em} were not reduced under any condition, the fluorescence recovery is attributed exclusively to the reversal of oxidation in Zr_{oxo}. Thus, the extent of optical restoration is directly correlated to the reducing capability of the solvent, reinforcing the redox-selective nature of coordination and fluorescence modulation in UiO-66-NH_2.

To evaluate the possibility of ligand detachment during the reduction process, ox-UiO-66-NH_2 was treated with MeOD, and the supernatant was analyzed via ^{1}H NMR spectroscopy (Figure S11). No distinct peaks corresponding to free BDC-NH_2 or BDC-NO_2 ligands were observed in the aromatic region (6−8 ppm), suggesting that no substantial ligand leaching occurred. However, based on our particle size (~640 nm), ligand density (~1.61 nm^{-2} for [100] and ~1.86 nm^{-2}), and estimated surface area (9.50×10^5 nm^2), we suspect that any partial detachment would yield a concentration below the NMR detection limit (typically ~10 μM at 400 MHz) and thus may remain undetectable under our experimental conditions.[53] This is further supported by bright-field (BF) microscopy, which showed no significant changes in morphology or size after the redox cycle. Nevertheless, the possibility of subtle surface coordination changes due to minor ligand detachment cannot be entirely excluded.

To investigate the impact of structural modifications induced by photooxidation and a change in coordination weakening of ligands, we conducted a series of Brunauer−Emmett−Teller (BET) measurements following the treatment of oxidized MOFs with various alcohols (Figure 5). During the oxidation of UiO-66-NH_2, a decrease in N_2 adsorption capacity was observed, accompanied by a sharp uptake at high relative pressures ($P/P_0 > 0.9$). This behavior is indicative of structural relaxation or partial framework collapse, leading to the formation of macropores and disordered domains. Such features are consistent with capillary condensation occurring within the enlarged or interconnected pore regions.

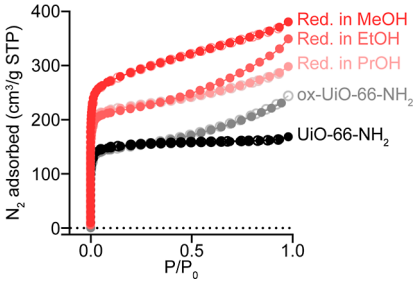

Figure 5. N_2 adsorption isotherms of UiO-66-NH_2 before and after photooxidation and alcohol-mediated reduction. Photooxidation decreases N_2 uptake and induces high-pressure uptake, suggesting structural relaxation. Alcohol treatment partially restores porosity, with MeOH yielding a higher uptake than UiO-66-NH_2, indicating redox-induced pore reorganization correlated with fluorescence recovery.

Subsequent reductive treatment with alcohols resulted in partial recovery of N_2 uptake. Notably, the extent of recovery correlated with the reducing strength of the alcohol used—MeOH exhibited the highest degree of restoration, followed by EtOH and PrOH. This trend paralleled the fluorescence recovery profile and supports the hypothesis that selective reduction of oxidized metal clusters reinstates metal−ligand coordination, thereby restoring both structural coordination weakening and porosity.

Interestingly, certain alcohol-treated samples exhibited N_2 adsorption capacities that exceeded that of pristine UiO-66-NH_2. This observation implies that the reductive process involves not only framework recovery but also structural reorganization, possibly through defect-assisted pore expansion. It is likely that previously oxidized and relaxed regions underwent redox-induced reconstruction, exposing new pore pathways or additional surface area. Such behavior aligns with redox-triggered framework remodeling, where partial lattice collapse is followed by recoordination and defect reconfiguration, ultimately enhancing accessible porosity beyond the original structure.

To confirm that the observed redox responsiveness originated from the electronic characteristics of the functional groups on the ligand, we conducted a control experiment using pristine UiO-66 without any substituents. Unlike UiO-66-NH_2, pristine UiO-66 does not exhibit any detectable fluorescence under visible-light irradiation, which limits optical tracking. Therefore, we employed N_2 adsorption−desorption measurements to investigate structural changes associated with redox treatments (Figure S12). Upon photooxidation, pristine UiO-66 exhibited a noticeable decrease in the pore volume, which is consistent with the oxidation of Zr_{oxo} domains or associated surface reorganization. However, subsequent exposure to ethanol did not induce any appreciable recovery in pore volume, in contrast to the functionalized analogues. This suggests that the presence of electron-donating ($-NH_2$) or -withdrawing ($-NO_2$) groups plays a critical role in enabling structural reversibility through redox processes.[54,55]

CONCLUSION

In this study, we elucidate how redox-mediated structural changes modulate the coordination and fluorescence of the prototypical MOF, UiO-66-NH_2. Upon visible-light irradiation, reactive oxygen species induce dual oxidation pathways: irreversible oxidation of L_{em} and reversible oxidation of M_{oxo}.

https://doi.org/10.1021/acsomega.5c05521
ACS Omega 2025, 10, 42882−42891

These processes result in a structural change and fluorescence quenching.

Selective reduction using alcohols enables partial restoration of structural coordination and fluorescence primarily through the reversible coordination of ox-Zr_{oxo}. The extent of fluorescence and porosity recovery strongly correlates with the reducing power and molecular size of the alcohols, indicating a structure−function relationship governed by redox-driven reconfiguration.

Notably, alcohol-treated samples exhibited enhanced porosity beyond that of the pristine MOF, suggesting that redox cycling can not only recover but also expand the structural architecture through defect reorganization and framework remodeling. These findings highlight a new design principle for MOFs, where reversible redox chemistry can be leveraged to dynamically tune the optical properties and structural accessibility. This strategy offers promising opportunities for the development of responsive, reconfigurable, and responsive MOF-based platforms for sensing, catalysis, and molecular transport.

■ ASSOCIATED CONTENT

Supporting Information

The Supporting Information is available free of charge at https://pubs.acs.org/doi/10.1021/acsomega.5c05521.

SEM image and photographs of UiO-66-NH_2; comparison of optical properties; ^{1}H NMR spectra; thermal imaging under irradiation; and comparison of fluorescence recovery in UiO-66-NH_2 (PDF)

■ AUTHOR INFORMATION

Corresponding Authors

Yongdeok Ahn − *Department of Physics and Chemistry, Daegu Gyeongbuk Institute of Science and Technology, Daegu 42988, Republic of Korea; Department of Chemistry, Pohang University of Science and Technology (POSTECH), Pohang 37673, Republic of Korea;* orcid.org/0000-0002-0422-0487; Email: ydahn@dgist.ac.kr

Daeha Seo − *Department of Physics and Chemistry, Daegu Gyeongbuk Institute of Science and Technology, Daegu 42988, Republic of Korea; Department of Chemistry, Pohang University of Science and Technology (POSTECH), Pohang 37673, Republic of Korea;* orcid.org/0000-0002-0454-1168; Email: livewire@dgist.ac.kr

Minyoung Yoon − *KNU G_LAMP Research Center, KNU Institute of Basic Science, Department of Chemistry, Kyungpook National University, Daegu 41566, Republic of Korea;* orcid.org/0000-0001-7436-6273; Email: myyoon@knu.ac.kr

Authors

Minsoo Park − *Department of Physics and Chemistry, Daegu Gyeongbuk Institute of Science and Technology, Daegu 42988, Republic of Korea*

Younghu Son − *KNU G_LAMP Research Center, KNU Institute of Basic Science, Department of Chemistry, Kyungpook National University, Daegu 41566, Republic of Korea*

Juhyeong Cho − *Department of Physics and Chemistry, Daegu Gyeongbuk Institute of Science and Technology, Daegu 42988, Republic of Korea*

Min Jeong Park − *KNU G_LAMP Research Center, KNU Institute of Basic Science, Department of Chemistry, Kyungpook National University, Daegu 41566, Republic of Korea*

Complete contact information is available at: https://pubs.acs.org/10.1021/acsomega.5c05521

Author Contributions

D. S., M. Y., and Y. A. designed experiments and conceptualized the project. M. P., J. C., and Y. A. performed general experiments, characterization of materials, and analysis of results. Y. S. and M. J. P. conducted the synthesis of materials. M. P., D. S., and M. Y. analyzed and discussed the results. M. P. and Y. A. visualized data and wrote the manuscript with input from all authors. D. S., M. Y., and Y. A. reviewed and edited manuscripts and supervised the research. All authors discussed the results and commented on the manuscript.

Notes

The authors declare no competing financial interest.

■ ACKNOWLEDGMENTS

This study is supported by the National Research Foundation of Korea (NRF) grants funded by the Korean Government (Ministry of Science and ICT, 2020M3A9D8038014, RS-2023-00252979), the DGIST Program of the MSIT (21-HRHR+-02) (D.S.), and the Global Learning and Academic Research Institution for Master's PhD students and Postdocs (LAMP) Program of the NRF grant funded by the Ministry of Education (No. RS-2023-00301914) (M.Y.). This work is also supported by POSTECH Basic Science Research Institute Grant, whose NRF grant number is RS-2021-NR060139 (D.S.). The authors thank the CCRF of DGIST for technical support with the fluorescence and electron microscopes.

■ ABBREVIATIONS

MOF, metal−organic frameworks; L_{em}, emissive ligand; RIM, restricted intramolecular motion; ROS, reactive oxygen species; M_{oxo}, metal-oxo clusters; PL, photoluminescence; MOF_{em}, emissive metal−organic frameworks; BDC-NH_2, 2-aminoterephthalic acid; Zr_{oxo}, $Zr_6O_4(OH)_4$; VB, valence band; CB, conduction band; ox-Zr_{oxo}, oxidation of Zr_{oxo}; ox-UiO-66-NH_2, oxidized UiO-66-NH_2; red-UiO-66-NH_2, reduced UiO-66-NH_2; XRD, X-ray diffraction; XPS, X-ray photoelectron spectroscopy; NHE, normal hydrogen electrode; FTIR, Fourier transform infrared; MeOH, methanol; EtOH, ethanol; PrOH, propanol; BET, Brunauer−Emmett−Teller measurement

■ REFERENCES

(1) Chakraborty, S.; Menon, D.; Mikulska, I.; Pfrang, C.; Fairen-Jimenez, D.; Misra, S. K.; Lynch, I. Make metal-organic frameworks safe and sustainable by design for industrial translation. *Nat. Rev. Mater.* **2025**, *10*, 167−169.

(2) Zhou, H.-C.; Long, J. R.; Yaghi, O. M. Introduction to metal-organic frameworks. *Chem. Rev.* **2012**, *112*, 673−674.

(3) Yang, Y.; Huang, L.; Wang, B.; Han, Y.; Shi, H.; Wei, L.; Guo, X.; Zhang, Y. Recent progress of separation and sensing applications of metal-organic framework-based membranes. *Chem. Eng. J.* **2025**, *506*, 160371.

(4) Han, X.; Chen, J.; Zhao, Y.; Kang, R.; Wei, Y.; Zhou, S. Dual antibody-guided delivery system using MOF-PQDs nanocomposites

for precise tumor diagnosis and combination therapy. *Chem. Eng. J.* **2025**, *505*, 159275.
(5) Venkateswarlu, S.; Reddy, A. S.; Panda, A.; Sarkar, D.; Son, Y.; Yoon, M. Reversible fluorescence switching of MOF nanoparticles: Security ink and ultrasensitive detection of Pb^{2+} ions in aqueous media. *ACS Appl. Nano Mater.* **2020**, *3* (4), 3684−3692.
(6) Zhu, X. D.; Zhang, K.; Wang, Y.; Long, W. W.; Sa, R. J.; Liu, T. F.; Lü, J. Fluorescent metal-organic framework (MOF) as a highly sensitive and quickly responsive chemical sensor for the detection of antibiotics in simulated wastewater. *Inorg. Chem.* **2018**, *57* (3), 1060−1065.
(7) Hu, Q.; Liu, J. L.; Zheng, Q. M.; Chang, J. F.; Wu, L. Z.; Zhang, M. D.; Qin, L. The ligand effect resulted in different fluorescence responses of two similar zinc-based MOFs to high-valence metal ions and amino acid Microporous. *Mesoporous Mater.* **2021**, *321*, 111130.
(8) Wang, Z.; Dai, B.; Su, Y.; Hu, H.; He, X.; Chen, J.; Wang, C. Why ligand doping increases the fluorescence of an anthracene-based metal-organic framework. *Inorg. Chem.* **2023**, *62* (30), 11809−11816.
(9) Sun, L.; Liu, Q.; Dang, S.; Jia, J. Highly luminescent lanthanide metal-organic frameworks for trace detection of norfloxacin. *Inorg. Chem.* **2025**, *64* (20), 10272−10278.
(10) Liu, S.; Cheng, Y.; Li, Y.; Chen, M.; Lam, J. W. Y.; Tang, B. Z. Manipulating solid-state intramolecular motion toward controlled fluorescence patterns. *ACS Nano* **2020**, *14* (2), 2090−2098.
(11) Li, Y.; Aquino, A. J. A.; Siddique, F.; Niehaus, T. A.; Lischka, H.; Nachtigallová, D. Pathways to fluorescence via restriction of intramolecular motion in substituted tetraphenylethylenes. *Phys. Chem. Chem. Phys.* **2022**, *24*, 1722−1735.
(12) Jin, K.; Park, N.; Ahn, Y.; Seo, D.; Moon, D.; Sung, J.; Park, J. Solvent-induced structural transformation in a one-dimensional coordination polymer. *Nanoscale* **2024**, *16*, 4571−4577.
(13) Kang, J.; Lhee, S. M.; Lee, J. K.; Zare, R. N.; Nam, H. G. Restricted intramolecular rotation of fluorescent molecular rotors at the periphery of aqueous microdroplets in oil. *Sci. Rep.* **2020**, *10*, 16859.
(14) Zhang, T.; Zhang, C.; Li, X.; Liang, M.; Bian, W.; Zhang, Y.; Wang, K.; Xue, P. Fluorescence response of cruciform D-π-A-π-D phenothiazine derivatives to mechanical force. *CrystEngComm* **2019**, *21*, 4192−4199.
(15) Güsten, H.; Meisner, R. Influence of restricted intramolecular motions on the fluorescence quantum yield of fluorophores. *J. Photochem.* **1983**, *21* (1), 53−60.
(16) Xu, C.; Shen, H.; Liu, T. M.; Kwok, R. T. K.; Lam, J. W. Y.; Tang, B. Z. Restriction of molecular motion to a higher level: Towards bright AIE dots for biomedical applications. *iScience* **2023**, *26* (5), 106568.
(17) Shu, Y.; Liu, X.; Zhang, M.; Liu, B.; Wang, Z. Deactivation of porphyrin metal-organic framework in advanced oxidation process: Photobleaching and underlying mechanism. *Appl. Catal., B* **2024**, *346*, 123746.
(18) Lee, K.; Shin, S.; Lee, W. J.; Choi, D.; Ahn, Y.; Park, M.; Seo, D.; Seo, K. Sunlight-activatable ROS generator for cell death using TiO_2/c-Si microwires. *Nano Lett.* **2021**, *21* (16), 6998−7004.
(19) Guo, L.; Liu, Y.; Qu, F.; Liu, Z.; Kong, R.; Chen, G.; Fan, W.; Xia, L. Luminescent metal organic frameworks with recognition sites for detection of hypochlorite through energy transfer. *Mikrochim. Acta* **2019**, *186* (11), 740.
(20) Katz, M. J.; Brown, Z. J.; Colon, Y. J.; Siu, P. W.; Scheidt, K. A.; Snurr, R. Q.; Hupp, J. T.; Farha, O. K. A facile synthesis of UiO-66, UiO-67 and their derivatives. *Chem. Commun.* **2013**, *49*, 9449−9451.
(21) Abid, H. R.; Shang, J.; Ang, H.; Wang, S. Amino-functionalized Zr-MOF nanoparticles for adsorption of CO_2 and CH_4. *Int. J. Smart Nano Mater.* **2013**, *4* (1), 72−82.
(22) Treger, M.; Hannebauer, A.; Schaate, A.; Budde, J. L.; Behrens, P.; Schneider, A. M. Tuning the optical properties of the metal-organic framework UiO-66- via ligand functionalization. *Phys. Chem. Chem. Phys.* **2023**, *25* (8), 6333−6341.
(23) Song, N.; Xing, C. C.; Li, D.; Zhang, P.; Zhai, Q. G. Regulation on the ligand fluorescence in UiO-66-Y metal-organic frameworks for effective detection of nitro-aromatic explosives. *J. Solid State Chem.* **2024**, *339*, 124972.
(24) Xu, F.; Zhang, J.; Zeng, X.; Long, Z.; Hou, X. UiO-66-NH_2: An easily attainable and label-free turn-on probe for facile fluorescence sensing of alkaline phosphatase. *Microchem. J.* **2022**, *179*, 107516.
(25) Wang, X.; Wang, X. UiO-66-NH_2 based fluorescent sensing for detection of tetracyclines in milk. *RSC Adv.* **2022**, *12* (36), 23427−23436.
(26) Zhang, S.; Xiao, J.; Zhong, G.; Xu, T.; Zhang, X. Design and application of dual-emission metal-organic framework-based ratiometric fluorescence sensors. *Analyst* **2024**, *149* (5), 1381−1397.
(27) Perego, J.; Bezuidenhout, C. X.; Villa, I.; Cova, F.; Crapanzano, R.; Frank, I.; Pagano, F.; Kratochwill, N.; Auffray, E.; Bracco, S.; Vedda, A.; Dujardin, C.; Sozzani, P. E.; Meinardi, F.; Comotti, A.; Monguzzi, A. Highly luminescent scintillating hetero-ligand MOF nanocrystals with engineered Stokes shift for photonic applications. *Nat. Commun.* **2022**, *13*, 3504.
(28) Dong, F.; Wang, X.; Zhao, Z.; Gao, S.; Wang, G.; Li, K.; Lin, Y. Ligand "lock and fix" strategy provides stability to metal-organic frameworks for photodegradation processes. *Cell Rep. Phys. Sci.* **2023**, *4* (9), 101545.
(29) Gayathri, K.; Vinothkumar, K.; Teja, Y. N.; Al-Shehri, B. M.; Selvaraj, M.; Sakar, M.; Balakrishna, R. G. Ligand-mediated band structure engineering and physiochemical properties of UiO-66 (Zr) metal-organic frameworks (MOFs) for solar driven degradation of dye molecules. *Colloids Surf., A* **2022**, *653*, 129992.
(30) Kessler, A.; Huang, P.; Blomberg, E.; Odnevall, I. Unravelling the mechanistic understanding of metal nanoparticle-induced reactive oxygen species formation: Insights from a Cu nanoparticle study. *Chem. Res. Toxicol.* **2023**, *36* (12), 1891−1900.
(31) Morris, T. W.; Wisman, D. L.; Din, N. U.; Le, D.; Rahman, T. S.; Tait, S. L. Tailoring the redox capabilities of organic ligands for metal-ligand coordination with vanadium single-sites. *Surf. Sci.* **2021**, *712*, 121888.
(32) Liu, Y.; Zhou, Y.; Tang, Q.; Li, Q.; Chen, S.; Sun, Z.; Wang, H. A direct Z-scheme Bi_2WO_6/NH_2-UiO-66 nanocomposite as an efficient visible-light-driven photocatalyst for NO removal. *RSC Adv.* **2020**, *10* (3), 1757−1768.
(33) Toe, C. Y.; Zheng, Z.; Wu, H.; Scott, J.; Amal, R.; Ng, Y. H. Photocorrosion of cuprous oxide in hydrogen production: Rationalising self-oxidation or self-reduction. *Angew. Chem., Int. Ed.* **2018**, *57* (41), 13613−13617.
(34) Ravi, K.; Bankar, B. D.; Jindani, S.; Biradar, A. V. Surfactant-assisted selective oxidation of aromatic amines to nitro compounds by in situ-formed performic acid. *ACS Omega* **2019**, *4* (5), 9453−9457.
(35) Giamello, E.; Murphy, D.; Garrone, E.; Zecchina, A. Formation of superoxide ions upon oxygen adsorption on magnesium doped magnesium oxide: An EPR investigation. *Spectrochim. Acta, Part A* **1993**, *49* (9), 1323−1330.
(36) Sinhamahapatra, A.; Jeon, J. P.; Kang, J.; Han, B.; Yu, J. S. Oxygen-deficient zirconia (ZrO_{2-x}): A new material for solar light absorption. *Sci. Rep.* **2016**, *6*, 27218.
(37) Shukla, A. K.; Verma, V.; Goriyan, P.; Rani, A.; Verma, A.; Singh, A.; Yadav, B. C.; Baimuratova, R. K.; Andreeva, A. V.; Dzhardimalieva, G. I. $Zr_6O_4(OH)_4$ based metal-organic frameworks for the enhanced chemiresistive sensing of ethanol. *J. Inorg. Organomet. Polym.* **2024**, *34*, 3457−3472.
(38) Das, R. S.; Warkhade, S. K.; Kumar, A.; Wankhade, A. V. Graphene oxide-based zirconium oxide nanocomposite for enhanced visible light-driven photocatalytic activity. *Res. Chem. Intermed.* **2019**, *45*, 1689−1705.
(39) Mazumder, A.; Sebastian, E.; Hariharan, M. Solvent dielectric delimited nitro-nitrito photorearrangement in a perylenediimide derivative. *Chem. Sci.* **2022**, *13* (30), 8860−8870.
(40) Carbonio, E. A.; Rocha, T. C. R.; Klyushin, A. Y.; Píš, I.; Magnano, E.; Nappini, S.; Piccinin, S.; Knop-Gericke, A.; Schlögl, R.; Jones, T. E. Are multiple oxygen species selective in ethylene epoxidation on silver? *Chem. Sci.* **2018**, *9* (4), 990−998.

https://doi.org/10.1021/acsomega.5c05521
ACS Omega 2025, 10, 42882−42891

(41) Liu, S.; Sun, C.; Chen, J.; Xiao, J.; Luo, J. L. A high-performance Ruddlesden-Popper perovskite for bifunctional oxygen electrocatalysis. *ACS Catal.* **2020**, *10* (22), 13437−13444.
(42) Jain, S.; Shah, J.; Negi, N. S.; Sharma, C.; Kotnala, R. K. Significance of interface barrier at electrode of hematite hydroelectric cell for generating ecopower by water splitting. *Int. J. Energy Res.* **2019**, *43* (9), 4743−4755.
(43) Liang, X.; Zhang, L.; Natarajan, S. K.; Becker, D. F. Proline mechanisms of stress survival. *Antioxid. Redox Signaling* **2013**, *19* (9), 998.
(44) Kramar, B. V.; Bondarenko, A. S.; Koehne, M. K.; Diroll, B. T.; Wang, X.; Yang, H.; Schanze, K. S.; Chen, L. X.; Tempelaar, R.; Hupp, J. T. Unexpected photodriven linker-to-node hole transfer in a zirconium-based metal-organic framework. *J. Phys. Chem. Lett.* **2024**, *15* (46), 11496−11503.
(45) Ahn, Y.; Park, J.; Park, M.; Jin, S.; Jo, W.; Kim, J.; Cho, S. H.; Seo, D. Combinatorial selective synthesis and excitation experiments for quantitative analysis of effect of Au on a semiconductor photocatalyst. *Chem* **2022**, *8* (9), 2485−2497.
(46) Ghobadi, E.; Marquardt, A.; Zirdehi, E. M.; Neuking, K.; Varnik, F.; Eggeler, G.; Steeb, H. The influence of water and solvent uptake on functional properties of shape-memory polymers. *Int. J. Polym. Sci.* **2018**, *2018* (1), 1−15.
(47) Wu, W.; Fan, J.; Wang, D.; Zhao, Y.; Zhao, X.; Wei, Y. Ultrathin UiO-66-NH_2 polycrystalline membrane for CO_2/CH_4 separation. *Carbon Capture Sci. Technol.* **2024**, *11*, 100183.
(48) Al-Jadir, T. M.; Siperstein, F. R. The influence of the pore size in metal-organic frameworks in adsorption and separation of hydrogen sulphide: A molecular simulation study. *Microporous Mesoporous Mater.* **2018**, *271*, 160−168.
(49) Rafiee, M.; Konz, Z. M.; Graaf, M. D.; Koolman, H. F.; Stahl, S. S. Electrochemical oxidation of alcohols and aldehydes to carboxylic acids catalyzed by 4-acetamido-TEMPO: an alternative to "Anelli" and "Pinnick" oxidations. *ACS Catal.* **2018**, *8* (7), 6738−6744.
(50) Yumura, T.; Amenomori, T.; Kagawa, Y.; Yoshizawa, K. Mechanism for the Formaldehyde to Formic Acid and the Formic Acid to Carbon Dioxide Conversions Mediated by an Iron-Oxo Species. *J. Phys. Chem. A* **2002**, *106* (4), 621−630.
(51) Altıncekic, N. G.; Lander, C. W.; Roslend, A.; Yu, J.; Shao, Y.; Noh, H. Electrochemically determined and structurally justified thermochemistry of H atom transfer on Ti-oxo nodes of the colloidal metal-organic framework Ti-MIL-125. *J. Am. Chem. Soc.* **2024**, *146* (40), 33485−33498.
(52) Kim, Y.; Smith, J. G.; Jain, P. K. Harvesting multiple electron-hole pairs generated through plasmonic excitation of Au nanoparticles. *Nat. Chem.* **2018**, *10*, 763−769.
(53) Lepucki, P.; Dioguardi, A. P.; Karnaushenko, D.; Schmidt, O. G.; Grafe, H. J. The normalized limit of detection in NMR spectroscopy. *J. Magn. Reson.* **2021**, *332*, 107077−107084.
(54) Vermoortele, F.; Vandichel, M.; Voorde, B. V.; Amellot, R.; Waroquier, M.; Speybroeck, V. V.; De Vos, D. E. Electronic effects of linker substitution on Lewis acid catalysis with metal organic framework. *Angew. Chem., Int. Ed.* **2012**, *51* (20), 4887−4890.
(55) Ji, P.; Drake, T.; Murakami, A.; Oliveres, P.; Skone, J. H.; Lin, W. Tuning Lewis acidity of metal-organic frameworks via perfluorination of bridging ligands: spectroscopic, theoretical, and catalytic studies. *J. Am. Chem. Soc.* **2018**, *140* (33), 10553−10561.

https://doi.org/10.1021/acsomega.5c05521
ACS Omega 2025, 10, 42882−42891